Fluor-rossmanite, □(Al₂Li)Al₆(Si₆O₁₈)(BO₃)₃(OH)₃F, a new tourmaline supergroup mineral from Malkhan pegmatite field, Western Siberia, Russia.

Anatoly V. Kasatkin[1], Fabrizio Nestola[2*], Maxwell C. Day[2], Liudmila A. Gorelova[3], Radek Škoda[4], Oleg S. Vereshchagin[3], Atali A. Agakhanov[1], Dmitriy I. Belakovskiy[1], Martha G. Pamato[2], Jan Cempírek[4] and Mikhail Yu. Anosov[1]

[1]Fersman Mineralogical Museum of the Russian Academy of Sciences, Leninsky Prospekt 18-2, 119071 Moscow, Russia;

[2]Dipartimento di Geoscienze, Università di Padova, Via Gradenigo 6, I-35131, Padova, Italy;

[3]Institute of Earth Sciences, St. Petersburg State University, University Emb. 7/9, 199034 Saint-Petersburg, Russia;

[4]Department of Geological Sciences, Faculty of Science, Masaryk University, Kotlářská 2, 611 37, Brno, Czech Republic

*Author for correspondence: Fabrizio Nestola, E-mail: fabrizio.nestola@unipd.it

Running title: Fluor-rossmanite, a new mineral

Abstract

Fluor-rossmanite, ideally □(Al₂Li)Al₆(Si₆O₁₈)(BO₃)₃(OH)₃F, is a new mineral of the tourmaline supergroup, found at the Krutaya pegmatite, Malkhan pegmatite field, Zabaykalskiy Krai, Western Siberia, Russia. It forms an intermediate zone up to 3 mm thick in a chemically heterogeneous, concentrically zoned, polychrome tourmaline crystal 3 x 2 cm in size. The new mineral is light pink, transparent with a white streak and a vitreous lustre. It is brittle, with conchoidal fracture. Mohs' hardness is 7. The $D_{meas} = 3.07(2)$ g cm^{-3} and $D_{calc} = 3.071$ g cm^{-3}. Optically, fluor-rossmanite is non-pleochroic, uniaxial (–), $\omega = 1.647(2)$, $\varepsilon = 1.628(2)$ (589 nm). The empirical formula calculated on the basis of 31 anions (O+OH+F) is: $^X(\square_{0.46}Na_{0.32}Ca_{0.20}Pb_{0.02})_{\Sigma1.00}{}^Y(Al_{1.84}Li_{1.05}Mn_{0.05}Fe^{2+}_{0.02}Ti_{0.02}Cr_{0.01})_{\Sigma2.99}{}^ZAl_{6.00}{}^T(Si_{5.79}Al_{0.21})_{\Sigma6.00}$ $B_{2.99}O_{27}{}^V(OH)_3{}^W[F_{0.44}(OH)_{0.20}O_{0.36}]_{\Sigma1.00}$. Fluor-rossmanite is trigonal, $R3m$; the unit-cell parameters are: $a = 15.7951(3)$, $c = 7.08646(17)$ Å, $V = 1531.11(7)$ Å^3, and $Z = 3$. The crystal
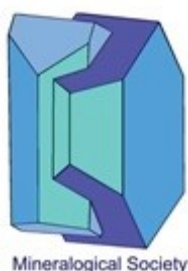
structure is refined from single-crystal X-ray diffraction data [R = 0.0211 for 1178 unique reflections with $I > 2\sigma(I)$]. The new mineral is a "fluor-" species belonging to the X-vacant group of the tourmaline supergroup. The closest end-member compositions of valid tourmaline species are those of rossmanite and fluor-elbaite, to which fluor-rossmanite is related by the substitutions $^W\text{F}^- \leftrightarrow {}^W\text{OH}^-$ and $^X2\square + {}^Y\text{Al}^{3+} \leftrightarrow {}^X2\text{Na}^+ + {}^Y\text{Li}^+$, respectively.

Keywords: fluor-rossmanite; new mineral species; crystal structure refinement; electron microprobe; infrared spectroscopy; Raman spectroscopy; tourmaline supergroup; Krutaya pegmatite; Malkhan pegmatite field.

Introduction

According to Henry *et al.* (2011), the general crystal-chemical formula of tourmaline supergroup minerals is written as $XY_3Z_6T_6O_{18}(BO_3)_3V_3W$. As of February 1$^{\text{st}}$ 2024, the supergroup included 39 valid members with the following species-defining components (The New International Mineralogical Association (IMA) List of Minerals, http://cnmnc.units.it/): X = Na, K, Ca and vacancy ($\square$); Y = Li, Mg, Mn^{2+}, Fe^{2+}, Al, V^{3+}, Cr^{3+}, Fe^{3+}, Ti; Z = Mg, Fe^{2+}, Al, V^{3+}, Cr^{3+}, Fe^{3+}; T = Si, Al; V = O, OH; W = O, OH, F. The dominance of specific ions at one or more structural sites gives rise to a range of distinct mineral species (Bosi *et al.*, 2022). Herein we describe a new, 40$^{\text{th}}$ member of the tourmaline supergroup named fluor-rossmanite (Russian cyrilic фторроссманит) in accordance with the current nomenclature of tourmaline-supergroup minerals (Henry *et al.*, 2011). The prefix "fluor-" indicates the monovalent substitution OH$^- \rightarrow$ F$^-$ at the W site in the root composition of rossmanite, $\square(\text{Al}_2\text{Li})\text{Al}_6(\text{Si}_6\text{O}_{18})(\text{BO}_3)_3(\text{OH})_3(\text{OH})$ (Selway *et al.*, 1998). The new mineral is defined as a fluor-species because F$^-$+OH$^-$ > O^{2-} and F$^-$ > OH$^-$ at the W site. It also belongs to the X-vacant group because $\square$ > Na$^+$ and $\square$ > Ca^{2+}+Pb^{2+} at the X site. The new mineral, its name and symbol (Frsm) have been approved by the Commission on New Minerals, Nomenclature and Classification of the IMA (IMA2023–111, Kasatkin *et al.*, 2024a). The holotype specimen is deposited in the systematic collection of the Fersman Mineralogical Museum of the Russian Academy of Sciences, Moscow with the registration number 6049/1.

Occurrence

Fluor-rossmanite was discovered at the Krutaya pegmatite ("жила Крутая" in cyrilic; 50°39'52" N, 109°55'35" E), Malkhan pegmatite field, Krasnochikoyskiy District, Zabaykalskiy Krai, Western Siberia, Russia (Fig. 1). The Malkhan pegmatite field covers an area of about 60

km^2 on the southern slopes of the Malkhan Ridge, at the interfluve of the Mogzon, Skakunia and Bolshaya Rechka rivers, which are the right tributaries of the Chikoi River. The Malkhan field was discovered by the "Baikalkvartzsamotsvety" geological expedition in 1983. Its uniqueness lies in its extraordinary abundance of pegmatite dikes containing semi-precious stones, primarily jewelry and collectible tourmaline. The Malkhan field contains > 300 pegmatites, 40 of which are tourmaline-rich (Peretyazhko *et al.*, 1989).

Geologically, the Malkhan pegmatite field occurs in the southwest region of the Caledonian Malkhan-Yablonovaya structural-formational zone. This uplifted area is bound by the Khilok deep fault to the north-northwest and the Chikoi deep fault to the south-southeast. These faults control related Mezozoic basins. More detailed data on the geology and mineralogy of the Malkhan pegmatite field is given by Altukhov *et al.* (1973), Badanina (1999), Peretyazhko *et al.* (1989), Vereshchagin *et al.* (2022), Zagorskiy (2010), Zagorskiy and Peretyazhko (1992a,b, 2006, 2008) and Zagorskiy *et al.* (1999).

The Krutaya pegmatite, where fluor-rossmanite was found, is one of the oldest-known in the Malkhan field. It was discovered by the geological expedition "Sosnovgeologiya" in 1981, *i.e.,* two years before the Malkhan field itself. However, the Krutaya pegmatite was studied much less than the Sosedka, Mokhovaya, Tabornaya, Oktyabrskaya and other world-famous pegmatite dikes that provided hundreds of first-class gem tourmaline specimens. Initial prospecting work in the mid-1980s revealed poor tourmaline mineralization and crystal quality in the Krutaya pegmatite. It is located 250 m northeast of the mouth of the Zapadnyi stream, it occurs in fine-grained gneiss-diorites and metagabbro and dips to the north-northeast at an angle of 60-70°, hence the name – Krutaya ("steep") – see Fig. 1. The pegmatite dike is 120 m long and up to 5 m thick with a poorly defined zonal structure. Most of the body is composed of graphic pegmatite, consisting of potassic feldspar, quartz, and albite. The central part of the pegmatite contains orange spessartine, muscovite, beryl and tourmaline in addition to individual miaroles (up to 0.3 x 0.2 m in size) lined with quartz crystals (Ivanov and Chuev, 2021). In 2020, the geological company LLC "Technologiya" resumed work on the pegmatite. Only very few crystals of gem-quality tourmaline were uncovered, one of which contained fluor-rossmanite. This crystal was obtained from the miners by one of the authors (Mikhail Yu. Anosov) during his trip to Zabaykalskiy Krai in October 2022.

Fluor-rossmanite is the fifth new mineral discovered at the Malkhan pegmatite field. These minerals include bismutocolumbite (Peretyazhko *et al.*, 1992), borocookeite (Zagorsky *et al.*, 2003), oxybismutomicrolite (Kasatkin *et al.*, 2020) and nioboixiolite-(Mn^{2+}) (Chukanov *et al.*, 2023).

3

General appearance, physical and optical properties

Fluor-rossmanite occurs as an intermediate light pink zone up to 3 mm thick in a chemically heterogeneous, concentrically zoned, polychrome tourmaline crystal 3.2 x 2 cm in size (Fig. 2). The above crystal is unique in terms of the quantity of tourmaline supergroup species it contains – we recorded as many as eight of them – and will be a subject of a special publication (Kasatkin *et al.*, 2024b). Here we report only briefly that its dark brown core consists of unusually Mn-rich (up to 9.60 wt.% MnO) fluor-tsilaisite with the average empirical formula $(Na_{0.50}Ca_{0.09}\square_{0.41})_{\Sigma1.00}(Al_{1.28}Mn^{2+}_{1.24}Li_{0.35}Ti_{0.06}Fe^{2+}_{0.03}Sc_{0.01}Cr_{0.01})_{\Sigma2.98}Al_{6.00}(Si_{5.79}Al_{0.21})_{\Sigma6.00}B_{2.99}O_{27}(OH)_3[F_{0.44}(OH)_{0.09}O_{0.47}]_{\Sigma1.00}$. Single local compositions corresponding to princivalleite and a potentially new tourmaline species, a Mn^{2+}-F-analogue of foitite with the end-member formula $\square(Mn_2Al)Al_6(Si_6O_{18})(BO_3)_3(OH)_3F$, are also recorded in this zone. The greenish-yellow intermediate zone consists of Mn-rich fluor-elbaite with the average chemical composition $(Na_{0.49}Ca_{0.15}\square_{0.36})_{\Sigma1.00}(Al_{1.53}Mn^{2+}_{0.84}Li_{0.55}Ti_{0.05}Fe^{2+}_{0.01}Sc_{0.01}Cr_{0.01})_{\Sigma3.00}Al_{6.00}(Si_{5.76}Al_{0.24})_{\Sigma6.00}B_{2.99}O_{27}[(OH)_{2.86}O_{0.14}]_{\Sigma3.00}(F_{0.52}O_{0.48})_{\Sigma1.00}$. Very few analyses of this zone correspond to the compositional field of darrellhenryite. This zone is surrounded by a Mn-poor, light pink zone composed mainly of fluor-rossmanite as described here. This zone also includes local chemical compositions corresponding to rossmanite and its oxy-analogue, another potentially new tourmaline species with the end-member formula $\square(Li_{0.5}Al_{2.5})Al_6(Si_6O_{18})(BO_3)_3(OH)_3O$. Finally, the yellowish-green peripheral zone consists of late-generation, Mn-bearing fluor-elbaite with the average empirical formula $(Na_{0.56}Ca_{0.11}\square_{0.33})_{\Sigma1.00}(Al_{1.75}Li_{0.90}Mn^{2+}_{0.24}Fe^{2+}_{0.06}Cr_{0.02}Ti_{0.02})_{\Sigma2.99}Al_{6.00}(Si_{5.82}Al_{0.18})_{\Sigma6.00}B_{3.00}O_{27}(OH)_3[F_{0.49}(OH)_{0.02}O_{0.49}]_{\Sigma1.00}$. From the center of the dark brown zone to the edge of the crystal, the Mn content decreases and the Li+Al content increases up to the middle of the pink zone where MnO reaches 0.21 wt.%. Subsequently, this compositional trend is reversed from the center of the pink zone to the edge of the crystal. Unfortunately, of the potentially new tourmaline species, only fluor-rossmanite formed monomineralic areas large enough such that it could be described as a valid mineral.

Fluor-rossmanite is pale pink, transparent, with white streak and vitreous lustre. It does not fluoresce under ultraviolet light. Cleavage and parting are not observed. Fluor-rossmanite is brittle with a conchoidal fracture. Its hardness on the Mohs scale based on scratch tests is 7. Its density measured by flotation in Clerici solution is 3.07(2) g cm^{-3}. A density value calculated using the empirical formula and the unit-cell parameters from single-crystal X-ray diffraction (XRD) data is 3.071 g cm^{-3}. In transmitted plane-polarized light fluor-rossmanite is non-pleochroic, uniaxial (–), $\omega = 1.647(2)$, $\varepsilon = 1.628(2)$ (589 nm).

4

Infrared spectroscopy

The Fourier-Transform InfraRed (FTIR) spectrum of fluor-rossmanite (Fig. 3) was collected using a Thermo Fisher Nicolet iN10 InfraRed microscope equipped with a KBr beam splitter and a LN-cooled MCT detector. The spectrum was collected at an operating resolution of 4 cm^{-1} over the range 4000–700 cm^{-1} by averaging 64 scans with a scan time of 5.6 seconds. Base-line corrections and peak identification were done using the OMNIC and Fityk V0.9.8 spectra software (Wojdyr, 2010). The FTIR spectrum of fluor-rossmanite was collected on an unoriented fragment of the X-ray crystal mounted on a BaF_2 background window.

A series of peaks is observed in the range ~3660-3320 cm^{-1} due to (OH) stretching modes associated with $^{O(1)}$(OH) and $^{O(3)}$(OH) where the O(1)-site is occupied by the W anions (OH)$^-$, F$^-$ and O^{2-} and the O(3) site is occupied by the V anion, (OH)$^-$. Each component band comprising the composite absorption in this region must be associated with the *nearest-neighbor* arrangements [1] *Y-Y-Y* – O(1) or [2] *Y-Z-Z* – O(3) (Bosi, 2013; Hawthorne, 2016; Bronzova *et al.*, 2019) where *Y* = Al^{3+} and Li^+ (and minor amounts of other cations), and *Z* = Al^{3+} in fluor-rossmanite. In the (OH)-stretching region of fluor-rossmanite, several relatively intense bands are observed at ≤ ~3600 cm^{-1}, such bands in tourmaline are generally attributed to local arrangements involving O(3) = (OH)$^-$ (Gonzalez-Carreño *et al.*, 1988; Bosi *et al.*, 2015; Hawthorne, 2016) the most abundant of which in fluor-rossmanite is likely Li-Al-Al-(OH). The bands observed at ≥ ~3600 cm^{-1} in the spectrum of fluor-rossmanite are associated with several distinct *Y-Y-Y* – O(1) arrangements where Y = Al^{3+} and Li^+. These bands are relatively weak, this is in accord with the (OH) contents of the O(1)-site compared to the O(3)-site. Absorption observed from 1420-1250 cm^{-1} and 1150-800 cm^{-1} is due to different symmetric and asymmetric stretching modes associated with $[BO_3]^{3-}$ and $[SiO_4]^{4-}$ groups, respectively. Absorption observed in the range 800-700 cm^{-1} is likely associated with *N*-O-*N* and O-*N*-O bending modes where *N* = Si, B, Al and Li (Mashkovtsev and Lebedev, 1991; Robert *et al.*, 1996). Absorbance due to atmospheric CO_2 transitions are observed in the range ~2370-2330 cm^{-1} and regions with relatively more noise observed at ~3900-3740 cm^{-1} and ~1740-1460 cm^{-1} are due to atmospheric contamination by H_2O vapor.

Raman spectroscopy

The Raman spectra of fluor-rossmanite (Fig. 4) were obtained from an oriented crystal (E // c and E ⊥ c) by using a Horiba Labram HR Evolution spectrometer. This dispersive, edge-filter-based system is equipped with an Olympus BX 41 optical microscope, a diffraction grating with 600 grooves per millimetre, and a Peltier-cooled, Si-based charge-coupled (CCD)

5

detector. The Raman spectra were collected using a 532 nm laser. The nominal laser beam energy of 50 mW was attenuated to 10% using a neutral density filter to prevent thermal damage of the analysed area. The Raman spectra were collected in the range of 80–4000 cm^{-1} using a 50× objective in confocal mode with a beam diameter was ~2.6 μm and an axial resolution ~5 μm. Time acquisition was 240 s per spectral window, 5 accumulations and 7 spectral windows were applied to cover the 80–4000 cm^{-1} range. Wavenumber calibration was done using the Rayleigh line and low-pressure Ne-lamp emissions. The wavenumber accuracy is ~0.5 cm^{-1}, and the spectral resolution is ~2 cm^{-1}. Band fitting was done after background correction using Voight functions and assuming combined Lorentzian-Gaussian band shapes (*PeakFit*; Jandel Scientific Software). Due to the presence of luminescence peaks in the Raman spectra of fluor-rossmanite, the sample was also analysed using a 473 nm laser to distinguish the Raman bands form the luminescence peaks.

Several Raman bands are observed in the (OH)-stretching region of fluor-rossmanite (Fig. 4). Where E ∥ c, bands are observed at 3469 cm^{-1}, 3596 cm^{-1}, 3652 cm^{-1}, and 3525 cm^{-1}. Where E ⊢ c, three relatively weaker bands are observed at 3473 cm^{-1}, 3594 cm^{-1}, and 3652 cm^{-1}, and the 3525 cm^{-1} band is not observed. The two most intense bands at 3469 cm^{-1} (3473 cm^{-1} for E ⊢ c) and 3596 cm^{-1} (3594 cm^{-1} for E ⊢ c) likely correspond to (OH)-stretching modes of the *Y-Z-Z* – O(3) arrangements; Al-Al-Al-(OH) and Li-Al-Al-(OH), respectively (Fantini *et al.*, 2014). The weaker band at 3652 cm^{-1} likely corresponds to the (OH)-stretching mode of the *Y-Y-Y* – O(1) arrangement; Li-Al-Al-(OH). The majority of bands in the lower frequency region from 80-1250 cm^{-1} correspond to vibrational modes associated with $[BO_3]^{3-}$ and $[SiO_4]^{4-}$ groups and $[Si_6O_{18}]^{12-}$ rings. Bands observed from ~800 – 1150 cm^{-1} correspond to different symmetric and antisymmetric Si-O and B-O stretching modes. Bands observed at < ~800 cm^{-1} correspond to many different vibrational modes that correspond to *N*-O-*N* and O-*N*-O bending modes where *N* = Si, B, Al, and Li. This region also contains bands due to vibrational modes associated with $[Si_6O_{18}]^{12-}$ rings (*e.g.,* ring breathing, puckering, and compression) and $[BO_3]^{3-}$ groups (Mihailova *et al.*, 1996; McKeown, 2008; Fantini *et al.*, 2014).

Chemical data

Chemical analyses (10 spots) were done with a JEOL JXA-8230 electron microprobe (WDS mode, 15 kV, 20 nA, 10 μm beam diameter). Special care was taken in measuring fluorine (F). A thorough F$K\alpha$ peak search was performed prior to the analysis. The use of TAP crystal made it possible to avoid the possible overlap of F$K\alpha$ line with Mn$L\alpha$ and Mn$L\beta$ lines and higher order Mn$K\alpha$ lines. The counting time for F was 60 s at the peak position and 30 s at

6

high- and low-energy backgrounds. Contents of other elements with atomic numbers higher than that of carbon are below detection limits. The raw intensities were processed for matrix effects using PAP correction algorithm (Pouchou & Pichoir, 1985). The theoretical amount of B_2O_3, H_2O and Li_2O were included in the computation.

Lithium and boron contents were determined by inductively coupled plasma – atomic emission spectroscopy (ICP-AES). For this purpose, 0.02 g of the sample was put into an EasyPrep iWave vessel where 2 ml of HNO_3, 3 ml of HCl and 5 ml of HF were added. The vessel was capped and placed in the MARS 6 iWave microwave for digestion at 200 °C for 4 hours. Upon digestion, the solution was left to cool at room temperature before being diluted to a final volume of 50 ml with de-ionized water. The solution was then filtered and analyzed with a Shimadzu ICPE-9820 atomic emission spectrometer with inductive coupled plasma. Water content was calculated from H content determined by CHNS-analysis carried out using a Thermo Flash 2000 organic elemental analyzer.

Analytical data are given in Table 1. The empirical formula calculated on the basis of 31 anions (O+OH+F) is: $(\square_{0.46}Na_{0.32}Ca_{0.20}Pb_{0.02})_{\Sigma1.00}(Al_{1.84}Li_{1.05}Mn^{2+}_{0.05}Fe^{2+}_{0.02}Ti_{0.02}Cr_{0.01})_{\Sigma2.99}Al_{6.00}(Si_{5.79}Al_{0.21})_{\Sigma6.00}$ $B_{2.99}O_{27}(OH)_3[F_{0.44}(OH)_{0.20}O_{0.36}]_{\Sigma1.00}$. The ideal formula is $\square(Al_2Li)Al_6(Si_6O_{18})(BO_3)_3(OH)_3F$ which requires Li_2O 1.61, B_2O_3 11.28, Al_2O_3 44.06, SiO_2 38.94, F 2.05, H_2O 2.92, O=F –0.86, total 100 wt.%. The Gladstone-Dale compatibility index $(1 - K_p/K_c)$ calculated for fluor-rossmanite using its empirical formula and the unit-cell parameters determined from single-crystal XRD data is 0.019 using D_{calc} and 0.018 using D_{meas}, both values rated as superior (Mandarino, 1981).

X-ray crystallography and crystal structure

Powder X-ray diffraction data (Table 2) were obtained using a DRON-2.0 diffractometer with Fe$K\alpha$ radiation, Mn-filter and quartz used as an internal standard. The instrument is installed at the Fersman Mineralogical Museum of Moscow (Russia). The parameters of the trigonal unit cell refined from the powder data using the UNITCELL software by Holland and Redfern (1997) are as follows: $a = 15.7846(13)$, $c = 7.0895(12)$ Å, $V = 1529.81(27)$ Å^3 and $Z = 3$.

Single-crystal X-ray diffraction (SXRD) analysis of fluor-rossmanite was done using a Supernova Rigaku-Oxford Diffraction diffractometer equipped with micro-source Mo$K\alpha$ radiation ($\lambda = 0.71073$ Å; 50 kV, 0.8 mA) and a Pilatus 200K Dectris detector at the University of Padova, Italy. The data were collected in 1638 frames over 33 runs; the exposure time was 7 seconds per frame for a total time of 12 hours and 17 minutes covering the full reciprocal

7

sphere up to $2\theta_{max} = 63.2°$ with a redundancy of 23.7 and 100% data completeness. The data were processed by *CrysAlisPro* 1.171.41.123a software (Rigaku Oxford Diffraction, 2018). The new mineral is trigonal, space group $R3m$, $a = 15.7951(3)$, $c = 7.08646(17)$ Å, $V = 1531.11(7)$ Å^3 and $Z = 3$.

The crystal structure of fluor-rossmanite was solved by direct methods and refined to $R_1 = 0.0211$ for 1178 unique reflections with $I > 2\sigma(I)$. The crystal data, data collection information, and structure refinement details are given in Table 3, atomic coordinates and equivalent anisotropic thermal parameters are reported in Table 4, whereas selected bond distances are provided in Table 5. The bond valence calculation is reported in Table 6. The crystallographic information file has been deposited with the Principal Editor of Mineralogical Magazine and is available as Supplementary material (see below).

The intensity data of fluor-rossmanite were processed and corrected for Lorentz, polarization, and background effects using CrysAlisPro 1.171.41.123a software. No violation of $R3m$ symmetry was detected. Structure refinement was done using the SHELXL-2019/3 program (Sheldrick, 2015). Starting coordinates were taken from Bosi *et al.* (2022). Variable parameters were scale factor, extinction coefficient, atom coordinates, site-scattering values (for the X and Y sites), and atomic-displacement factors. The absorption correction was carried out by the interframe scaling (CrysAlis Pro 1.171.41.123a). Neutral scattering factors were used for the cations and oxygen atoms. As for the atomic model refinement, the X site was refined using the Na scattering factor; the Y site was refined using the Al scattering factor. The occupancies of Z and B sites were not refined because of their full occupancies from the chemical composition (e.g., ^{Z}Al = 6 a.p.f.u. and B = 2.99 a.p.f.u.). For the T site, we preferred to fix its occupancy to the chemical composition to avoid refinement of Si versus Al, which would not provide reliable results by X-ray diffraction.

In terms of site occupancy, the observed mean atomic number (M.A.N.; the value is referred to electrons) obtained by the chemical composition at the X and Y sites are 9.16 and 9.87, respectively. The refined M.A.N. from the crystal structure data for the X site is 9.59, which is in good agreement with the EMPA data with a difference of only 4.5%, slightly better that the rossmanite refinement (Selway *et al.*, 1998), where the difference between the refined M.A.N. and the EMPA data is 6%. Such small discrepancies could be reasonable considering that the X sites in rossmanite and fluor-rossmanite are largely vacant. For the Y site, the refined M.A.N. from the crystal structure data for fluor-rossmanite is 9.93, which is also in good agreement with the EMPA data (9.87). These observations definitively indicate that the chemical composition provided for fluor-rossmanite is accurate. To better show this, we performed the bond valence calculation (Table 6) in order to apply the equation for the F, OH,

8

O distribution at the W site (Bosi, 2013). This equation is given as follows: $^W(OH) = 2 - [1.01$ x BVS(F1)] - 0.21 - F. The original equation reports O1 instead of F1 but for fluor-rossmanite we indicated this site as F1. Using our experimental F content from the fluor-rossmanite formula, which is 0.44 a.p.f.u., and the bond-valence sum (BVS) at F1, which is ~1.17 vu, we obtain OH = 0.18 a.p.f.u. compared to the experimentally determined value of 0.20. Thus, using the above equation, we get the following W site occupancy: $^W[F_{0.44}(OH)_{0.29}O_{0.27}]$. The occupancy obtained experimentally from the chemical analyses is as follows: $^W[F_{0.44}(OH)_{0.20}O_{0.36}]$. Although differences between the calculated and experimental W site occupancy are observed, in both the cases, we confirm that F dominates the W position and that F + OH > O, which are the required conditions to use the prefix "fluor-" in "fluor-rossmanite".

With regards to the crystal structure of fluor-rossmanite, a direct comparison can be made with rossmanite (Selway *et al*., 1998). The unit-cell volume of rossmanite is slightly smaller (V ≈ 1531 Å^3 fluor-rossmanite, V ≈ 1526 Å^3 rossmanite); the main reason for this difference is made apparent by comparison of the bond lengths in each mineral. With regards to the X site, <X-O> = 2.678 Å in fluor-rossmanite compared to 2.666 Å in rossmanite. With regards to the Y site, <Y-O> = 1.985 Å in fluor-rossmanite compared to 1.966 Å in rossmanite. As expected, <Z-O> distances are practically identical for both rossmanite and fluor-rossmanite (1.904 and 1.905 Å, respectively) and consistent with the Z site occupied solely by Al (e.g., Kutzschbach *et al*., 2017; Vereshchagin *et al*., 2018; Bačík, 2018). We observe the same for the B site, which shows an average value of 1.371 Å for rossmanite and fluor-rossmanite. The situation is the same for the T site with an average value of 1.614 Å for both the minerals, which indicates a slight inclusion of aluminum in the TO$_4$ tetrahedron (e.g., Vereshchagin *et al*., 2024). To conclude, the larger unit-cell volume of fluor-rossmanite with respect to that of rossmanite is mainly related to the Y site as fluor-rossmanite has a <Y-O> almost 1% larger than in rossmanite. This is due to differences in the occupancy of the Y site, which shows an average cation radii of 0.618 Å in fluor-rossmanite compared to 0.597 Å in rossmanite (Shannon, 1976).

End-member formula and relation to other species

Within the tourmaline supergroup (Henry *et al*., 2011), fluor-rossmanite belongs to the X-site vacant tourmaline group and at the lower hierarchical level – to the vacant-subgroup 2. During the CNMNC voting procedure on fluor-rossmanite, several voting members expressed their concern about its validity as a new species because the total charge at the X site in the empirical formula (+0.76) appears to be closer to 1 than 0. It should be noted that according to Bosi *et al.* (2019), this value can deviate from the correct value due to a lack of consideration of all the potential end-members involved in chemical substitution. In our case, the occurrence

9

of Ca^{2+} and Pb^{2+}, for example, via the substitution $Ca(Pb) + Li \rightarrow \square + Al$, affects the total charge at the X-site. Based on the empirical formula, several end-member charge arrangements can be written such as:

1) $[^X(0)\ ^Y(1^+3^+_2)\ ^Z(3^+)_6\ (^T4^+_6 2^-_{18})\ (^B3^+2^-_3)_3\ ^V(1^-)_3\ ^W(1^-)]_{0.46}$ limited by vacancy content;

2) $[^X(1^+)\ ^Y(1^+3^+_2)\ ^Z(3^+)_6\ (^T4^+_6 2^-_{18})\ (^B3^+2^-_3)_3\ ^V(1^-)_3\ ^W(2^-)]_{0.32}$ limited by 1^+-cations content;

3) $[^X(1^+)\ ^Y(1^+_{1.5}3^+_{1.5})\ ^Z(3^+)_6\ (^T4^+_6 2^-_{18})\ (^B3^+2^-_3)_3\ ^V(1^-)_3\ ^W(1^-)]_{0.32}$ limited by 1^+-cations content;

4) $[^X(2^+)\ ^Y(1^+_2 3^+)\ ^Z(3^+)_6\ (^T4^+_6 2^-_{18})\ (^B3^+2^-_3)_3\ ^V(1^-)_3\ ^W(1^-)]_{0.22}$ limited by 2^+-cations content.

The prevailing charge arrangement is the first one, which aligns with the end-member composition of fluor-rossmanite as $^X\square\ ^Y(Al_2Li)\ ^ZAl_6(^TSi_6O_{18})(BO_3)_3\ ^V(OH)_3\ ^WF$.

Fractions of individual end-members of the studied tourmaline can be deciphered from its empirical formula by repetitive extraction of the dominant end-member and subsequent application of classification procedures (Bosi *et al.*, 2019) to the remaining composition. Apart from dominant fluor-rossmanite (46 mol.%) component, the other participating end-members include darrellhenryite (32 mol.%), liddicoatite (13.5 mol.%) and several other end-member compositions in quantity <5 mol.% each (Table 7).

Fluor-rossmanite is related to rossmanite (Selway *et al.*, 1998) by the monovalent substitution $^WF^- \leftrightarrow ^WOH^-$ and to fluor-elbaite, $Na(Li_{1.5}Al_{1.5})Al_6(Si_6O_{18})(BO_3)_3(OH)_3F$ (Bosi *et al.*, 2013) by the heterovalent substitution $^X2\square + ^YAl^{3+} \leftrightarrow ^X2Na^+ + ^YLi^+$. Alumino-oxy-rossmanite, $\square Al_3Al_6(Si_5AlO_{18})(BO_3)_3(OH)_3O$ (Ertl *et al.*, 2022) can be derived from fluor-rossmanite by the substitution $^YLi^+ + ^W2F^- \leftrightarrow ^YAl^{3+} + ^W2O^{2-}$ leading to a potentially new "oxy-rossmanite" species, $\square(Al_{2.5}Li_{0.5})Al_6(Si_6O_{18})(BO_3)_3(OH)_3O$ and then by $^YLi^+ + ^T2Si^{4+} \leftrightarrow ^YAl^{3+} + ^T2Al^{3+}$.

Fluor-rossmanite is the seventh member of the tourmaline supergroup with a dominantly vacant X site along with rossmanite, $\square(LiAl_2)Al_6(Si_6O_{18})(BO_3)_3(OH)_3(OH)$ (Selway *et al.*, 1998), foitite, $\square(Fe^{2+}_2Al)Al_6(Si_6O_{18})(BO_3)_3(OH)_3(OH)$ (MacDonald *et al.*, 1993), magnesio-foitite, $\square(Mg_2Al)Al_6(Si_6O_{18})(BO_3)_3(OH)_3(OH)$ (Hawthorne *et al.*, 1999), oxy-foitite, $\square(Fe^{2+}Al_2)Al_6(Si_6O_{18})(BO_3)_3(OH)_3O$ (Bosi *et al.*, 2017), celleriite $\square(Mn^{2+}_2Al)Al_6(Si_6O_{18})(BO_3)_3(OH)_3(OH)$ (Bosi *et al.*, 2022) and alumino-oxy-rossmanite, $\square Al_3Al_6(Si_5AlO_{18})(BO_3)_3(OH)_3O$ (Ertl *et al.*, 2022).

However, fluor-rossmanite is the first species with simultaneous dominance of vacancy at the X site and F at the W site. Henry (2005) and Henry and Dutrow (2011) observed the general aversion to $^X\square - ^WF$ in empirical data of tourmalines; they suggested that it is caused by a combination of both F concentrations in the coexisting fluid and crystallographic factors. The

10

W site which exclusively hosts F, is coordinated by three *Y* site cations; bond valence requirements related to the short-range ordering of F suggest that it should be present at the W site only if the average charge at the three *Y* sites is below +7. On the other hand, *X*-site vacancy typically compensates substitution of Al^{3+} at the Y site which increases the total charge at the *Y* sites. Therefore, the presence of ^{X}Ca in fluor-rossmanite may act to reduce the charge at the *Y*-site. A Y site charge of +6.82, calculated from the empirical formula of fluor-rossmanite, is close to the structural limit although structural strain is partially relaxed by the presence of ^{T}Al. The most important geochemical factor related to the aversion of tourmaline to $^X\square-^WF$, is the gradual increase of alkalinity together with F contents in pegmatite melts. This results in the typical evolution of tourmaline composition from foitite to schorl, elbaite, fluor-elbaite and fluor-liddicoatite (e.g., Selway *et al.*, 1999; Henry and Dutrow, 2011). This trend is partially broken in the final stage of tourmaline crystallization when both Na and F contents in tourmaline decrease (the *"darrellhenryite loop"*; Skřápková *et al.*, 2017) before their renewed increase in the final stage of magmatic crystallization. This decrease in Na and F is explained either by crystallization of other F-rich phases in the system, e.g. Li-mica, or by fluid exsolution after pocket rupture and system opening (e.g. Henry and Dutrow 2011, Bosi *et al.*, 2022).

Supplementary material

To view supplementary material for this article, please visit: https://doi.org/...

Competing interests.

The corresponding author (FN) is a guest member of the editorial board of Mineralogical Magazine for the special issue "Mineralogy, petrology and geochemistry of pegmatites". The peer-review process was guided by an independent editor, and the authors also have no other competing interests to declare.

References

Adams St. (2001) Relationship between bond valence and bond softness of alkali halides and chalcogenides. *Acta Crystallographica*, **B57**, 278–287.

Allmann R. (1975) Relations between bond lengths and bond strengths in oxide structures. *Monatshefte für Chemie*, **106**, 779–793.

Altukhov E.N., Smirnov A.D. and Leontiev L.N. (1973) Tectonics of Transbaikalia. Moscow: Nedra, 172 p. (in Russian).

Bačík, P. (2018) The crystal-chemical autopsy of octahedral sites in Na-dominant tourmalines: Octahedral metrics model unconstrained by the Y, Z-site disorder assignment. *Journal of Geosciences,* **63**, 137–154.

Badanina E.V. (1999) Tectonics of Transbaikalia. Mineralogical and geochemical features of pegmatites of the Malkhan gemstone deposit, Central Transbaikalia (as an example of pegmatites of the Phanerozoic tectono-magmatic activation zones). Ph. D. Thesis. Saint Petersburg, 202 p. (in Russian).

Bosi F. (2013) Bond-valence constraints around the O1 site of tourmaline. *Mineralogical Magazine*, **77**, 343–351.

Bosi F., Andreozzi G.B., Skogby H., Lussier A.J., Abdu Y. and Hawthorne, F.C. (2013) Fluor-elbaite, $Na(Li_{1.5}Al_{1.5})Al_6(Si_6O_{18})(BO_3)_3(OH)_3F$, a new mineral species of the tourmaline supergroup. *American Mineralogist*, **98**, 297–303.

Bosi F., Skogby H., Lazor P. and Reznitskii L. (2015) Atomic arrangements around the O3 site in Al- and Cr-rich oxy-tourmalines: a combined EMP, SREF, FTIR and Raman study. *Physics and Chemistry of Minerals*, **42**, 441–453.

Bosi F., Skogby H. and Hålenius U. (2017) Oxy-foitite, $\square(Fe^{2+}Al_2)Al_6(Si_6O_{18})(BO_3)_3(OH)_3O$, a new mineral species of the tourmaline supergroup. *European Journal of Mineralogy*, **29**, 889–896.

Bosi F., Biagioni C. and Oberti R. (2019) On the Chemical Identification and Classification of Minerals. *Minerals*, **9**, 591.

Bosi F., Pezzotta F., Skogby H., Altieri A., Hålenius U., Tempesta G. and Cempírek J. (2022) Princivalleite, $Na(Mn_2Al)Al_6(Si_6O_{18})(BO_3)_3(OH)_3O$, a new mineral species of the

tourmaline supergroup from Veddasca Valley, Varese, Italy. *Mineralogical Magazine*, **86**, 78–86.

Bosi F., Pezzotta F., Altieri A., Andreozzi G. B., Ballirano, P., Tempesta G., Cempírek J., Škoda R., Filip J., Čopjaková R., Novák M., Kampf A.R., Scribner E.D., Groat L.A. and Evans R.J. (2022). Celleriite, $\square(Mn_2^{2+}Al)Al_6(Si_6O_{18})(BO_3)_3(OH)_3(OH)$, a new mineral species of the tourmaline supergroup. *American Mineralogist*, **107**, 31–42.

Brese N.E. and O'Keeffe M.O. (1991) Bond-valence parameters for solids. *Acta Crystallographica*, **B47**, 192–197.

Bronzova Y., Babushkina M., Frank-Kamenetskaya O., Vereshchagin O., Rozhdestvenskaya I., Zolotarev A. (2019) Short-range order in Li–Al tourmalines: IR spectroscopy, X-ray single crystal diffraction analysis and a bond valence theory approach. *Physics and Chemistry of Minerals,* **46**, 815–825.

Brown I.D. and Altermatt D. (1985) Bond-valence parameters obtained from a systematic analysis of the Inorganic Crystal Structure Database. *Acta Crystallographica*, **B41**, 244–247.

Cabana J., Ling C.D., Oro-Sole J., Gautier D., Tobias G., Adams S., Canadell E. and Palacin M.R. (2004) Antifluorite-Type Lithium Chromium Oxide Nitrides: Synthesis, Structure, Order, and Electrochemical Properties. *Inorganic Chemistry*, **43**(22), 7050–7060.

Chukanov N.V., Pekov I.V., Zubkova N.V., Yapaskurt V.O., Shelukhina Yu.S., Britvin S.N. and Pushcharovsky D.Yu. (2023) Nioboixiolite-(Mn^{2+}), $(Nb_{2/3}Mn^{2+}_{1/3})O_2$, a New Ixiolite-Group Mineral from the Malkhan Pegmatite Field, Transbaikal Region, Russia. *Zapiski RMO*, **152**(1), 8–17.

Czerwinska K., Madura I.D. and Zachara J. (2016) Geometry of trigonal boron coordination sphere in boronic acids derivatives – a bond-valence vector model approach. *Acta Crystallographica*, **B72**, 241–248.

Ertl A., Hughes J.M., Prowatke S., Ludwig T., Lengauer C.L., Meyer H.P., Giester G., Kolitsch U. and Prayer A. (2022) Alumino-oxy-rossmanite from pegmatites in Variscan metamorphic rocks from Eibenstein an der Thaya, Lower Austria, Austria: A new tourmaline that represents the most Al-rich end-member composition. *American Mineralogist*, **107**, 157–166.

Fantini C., Tavares M.C., Krambrock K., Moreira R.L. and Right A. (2014) Raman and infrared study of hydroxyl sites in natural uvite, fluor-uvite, magnesio-foitite, dravite and elbaite tourmalines. *Physics and Chemistry of Minerals*, **41**, 247–254.

Gagné O.C. and Hawthorne F.C. (2015) Comprehensive derivation of bond-valence parameters for ion pairs involving oxygen. *Acta Crystallographica*, B**71**, 561–578.

Gonzales-Carreño T., Fernández M. and Sanz J. (1988) Infrared and electron microprobe analysis of tourmaline. *Physics and Chemistry of Minerals*, **15**, 452–460.

Hawthorne F.C. (2016) Short-range atomic arrangements in minerals. I: The minerals of the amphibole, tourmaline and pyroxene supergroups. *European Journal of Mineralogy*, **28**, 513–536.

Henry D. J. (2005) Fluorine–X-site vacancy avoidance in natural tourmaline: internal vs. external control. *Geochimica et Cosmochimica Acta* **69**, A25–A25.

Henry D. J. and Dutrow B. L. (2011) The incorporation of fluorine in tourmaline: Internal crystallographic controls or external environmental influences? *The Canadian Mineralogist*, **49**, 41–56.

Henry D.J., Novák M., Hawthorne F.C., Ertl, A., Dutrow B.L., Uher P. and Pezzotta F. (2011) Nomenclature of the tourmaline-supergroup minerals. *American Mineralogist,* **96**, 895–913.

Holland T.J.B. and Redfern S.A.T. (1997) Unit cell refinement from powder diffraction data: the use of regression diagnostics. *Mineralogical Magazine*, **61**, 65–77.

Ivanov P.F. and Chuev S.A. (2021) Report on prospecting works for tourmaline in the Malkhan pegmatite field, Pravoberezhniy, Levoberezhniy and Verkhnemogzonskiy areas in the Krasnochikoysk district of the Transbaikal Krai in 2018–2020 with the calculation of reserves as of 01.01.2021. Ulan-Ude, 221 p. (in Russian).

Kanowitz S.M. and Palenik G.J. (1998) Bond Valence Sums in Coordination Chemistry Using Oxidation-State-Independent R0 Values. A Simple Method for Calculating the Oxidation State of Iron in Fe−O Complexes. *Inorganic Chemistry*, **37**(8), 2086-2088.

Kasatkin A.V., Britvin S.N., Peretyazhko I.S., Chukanov N. V., Škoda R. and Agakhanov A.A. (2020) Oxybismutomicrolite, a new pyrochlore-supergroup mineral from the Malkhan pegmatite field, Central Transbaikalia, Russia, *Mineralogical Magazine,* **84**, 444–454.

Kasatkin A.V., Nestola F., Day M.C., Gorelova L.A., Škoda R., Vereshchagin O.S., Agakhanov A.A. and Belakovskiy D.I. (2024a) Fluor-rossmanite, IMA 2023-111. CNMNC Newsletter 78, *European Journal of Mineralogy*, **36**, https://doi.org/10.5194/ejm-36-361-2024, 2024.

....

Kasatkin A.V., Vereshchagin O.S., Gorelova L.A., Belakovskiy D.I. (2024b) Eight mineral species in one crystal: unique zonation of polychrome tourmaline from the Krutaya vein (Malkhan pegmatite field, Transbaikalia). *Mineralogy,* **10** (2), DOI: 10.35597/2313-545X-2024-10-2-1 (in Russian).

14

Krivovichev S.V. and Brown I.D. (2001) Are the compressive effects of encapsulation an artifact of the bond valence parameters? *Zeitschrift für Kristallographie*, **216**, 245–247.

Kutzschbach M., Wunder B., Krstulovic M., Ertl A., Trumbull R., Rocholl A., Giester G. (2017) First high-pressure synthesis of rossmanitic tourmaline and evidence for the incorporation of Li at the X site. *Physics and Chemistry of Minerals*, **44**, 353–363

Liu W. and Thorp H.H. (1993) Bond valence sum analysis of metal-ligand bond lengths in metalloenzymes and model complexes. 2. Refined distances and other enzymes. *Inorganic Chemistry*, **32**, 4102–4105.

MacDonald D.J., Hawthorne F.C. and Grice J.D. (1993) Foitite, $\square Fe^{2+}_2(Al,Fe^{3+})Al_6Si_6O_{18}(BO_3)_3(OH)_4$, a new alkali-deficient tourmaline: Description and crystal structure. *American Mineralogist*, **78**, 1299–1303.

Mandarino J.A. (1981) The Gladstone-Dale relationship. IV. The compatibility concept and its application. *Canadian Mineralogist*, **41**, 989–1002.

Mashkovtsev R.I. and Lebedev A.S. (1991) IR-spectroscopy of OH-groups in tourmaline. *Soviet Geology and Geophysics*, **32**, 80–84.

McKeown D.A. (2008) Raman spectroscopy, vibrational analysis, and heating of buergerite tourmaline. *Physics and Chemistry of Minerals*, **35**, 259–270.

Mihailova B., Gasharova B. and Konstantinov L. (1996) Influence of Non-Tetrahedral Cations on Si-O Vibrations in Complex Silicates. *Journal of Raman Spectroscopy*, **27**, 829–833.

Pouchou J.L. and Pichoir F. (1985) 'PAP' u(qZ) procedure for improved quantitative microanalysis. In Microbeam Analysis (J.T. Armstrong, ed.). San Francisco Press, San Francisco, California, United States (104–106).

Peretyazhko I.S., Zagorskiy V.E. and Bobrov Y.D. (1989) First find of Bi- and Pb-rich tourmalines. *Doklady AN SSSR*, **307**(6), 1461–1465 (in Russian).

Peretyazhko I.S., Zagorskiy V.E., Sapozhnikov A.N., Bobrov Y.D. and Rakcheev A.D. (1992) Bismutocolumbite $Bi(Nb,Ta)O_4$ – a new mineral from miarolitic pegmatites. *Zapiski VMO*, **121**(3), 130–134 (in Russian).

Rigaku Oxford Diffraction, *CrysAlisPro Software system, version 1.171.41.123a*, 2022.

Robert J.-L., Fuchs Y. and J.-P. Gourdant (1996) Characterization of tourmalines by FTIR absorption spectrometry. *Physics and Chemistry of Minerals*, **23**(4/5), 309.

Selway J.B., Novák M., Hawthorne F.C., Černý P., Ottolini L. and Kyser T.K. (1998) Rossmanite, $\square(LiAl_2)Al_6(Si_6O_{18})(BO_3)_3(OH)_4$, a new alkali-deficient tourmaline: description and crystal structure. *American Mineralogist,* **83**, 896–900.

15

Selway J.B., Novak M., Černý P. and Hawthorne F.C. (1999). Compositional evolution of tourmaline in lepidolite-subtype pegmatites. *European Journal of Mineralogy*, **11**, 569–584.

Shannon R.D. (1976) Revised effective ionic radii and systematic studies of interatomic distances in halides and chalcogenides. *Acta Crystallographica*, **A32**, 751–767.

Sheldrick G.M. (2015) Crystal structure refinement with SHELXL. *Acta Crystallographica*, **C71**, 3–8.

Skřápková L., Cempírek J. and Vašinová Galiová M. (2017) Fractionation in Li-tourmaline from the Lhenice lepidolite pegmatite – "darrellhenryite loop" in F-saturation. In (Eds. Cempírek et al.) Book of abstracts to Tourmaline 2017 International symposium, Skalský Dvůr, Czech Republic, 79–80.

Urusov V.S. (2006) Problem of optimization of bond valence model parameters (as exemplified by managanese in different oxidation states). *Doklady Physical Chemistry*, **408**, 152–155.

Vereshchagin O.S., Kasatkin A.V. and Škoda R. (2022) New data on Bi-, Pb-bearing and Mn-rich gem tourmaline from the Malkhan pegmatite district (Transbaikalia). *Zapiski RMO*, **151**(6), 46–57.

Vereshchagin O.S., Frank-Kamenetskaya O.V., Rozhdestvenskaya I.V., Zolotarev A.A. (2018) Incorporation of 3d elements in tourmalines: Structural adjustments and stability. *European Journal of Mineralogy*, **30 (5)**, 917–928.

Vereshchagin O.S., Gritsenko Yu.D., Vigasina M.F., Dedushenko S.K., Gorelova L.A., Pautov L.A., Agahanov A.A., Chernyshova I.A., Zolotarev A.A. (2024) Tetrahedral aluminum in tourmaline from a spinel-pargasite-metamorphosed mafic ultramafic rock. *American Mineralogist* (in press). https://doi.org/10.2138/am-2023-9170Wojdyr M. (2010) Fityk: a general-purpose peak fitting program. *Journal of Applied Crystallography*, **43**, 1126–1128.

Wojdyr M. (2010) Fityk: a general purpose peak fitting program. *Journal of Applied Crystallography*, **43**, 1126-1128.

Wood R.M. and Palenik G.J. (1999) Bond valence sums in coordination chemistry. Sodium-Oxygen Complexes. *Inorganic Chemistry*, **38**(17), 3926–3930.

Yu D. and Xue D. (2006) Bond analyses of borates from the Inorganic Crystal Structure Database. *Acta Crystallographica*, **B62**, 702–709.

Zagorskiy V.E. (2010) Malkhan deposit of tourmalines: types and origin of miaroles. *Doklady RAN*, **431**(1), 81–84 (in Russian).

Zagorskiy V.E. and Peretyazhko I.S. (1992a) Gem pegmatites of Central Transbaikalia. Novosibirsk: Nauka, 224 p. (in Russian).

Zagorskiy V.E. and Peretyazhko I.S. (1992b) Types and mean composition of miarolitic pegmatites of Malkhan ridge. *Geology and Geophysics*, **1**, 87–98 (in Russian).

Zagorskiy V.E. and Peretyazhko I.S. (2006) Malkhan granite-pegmatite system. *Doklady RAN*, **406**(4), 511–515 (in Russian).

Zagorskiy V.E. and Peretyazhko I.S. (2008) The Malkhan Gem Tourmaline Deposit in Transbaikalia, Russia. *Mineralogical Almanac*, **13b**, 4–41.

Zagorskiy V.E., Peretyazhko I.S. and Shmakin B.M. (1999) Granite pegmatites. Vol. 3. Miarolitic pegmatites. Novosibirsk: Nauka, 485 p. (in Russian).

Zagorsky V.Y., Peretyazhko I.S., Sapozhnikov A.N., Zhukhlistov A.P. and Zvyagin B.B. (2003) Borocookeite, a new member of the chlorite group from the Malkhan deposit, Central Transbaikalia, Russia. *American Mineralogist*, **88**, 830–836.

17

Table 1. Chemical composition of fluor-rossmanite

Constituent	Wt.%	Range	Stand. Dev.	Probe Standard
SiO_2	36.70	36.27 – 37.00	0.22	Jadeite
TiO_2	0.20	0.14 – 0.24	0.03	$MnTiO_3$
B_2O_3*	10.98			Inorganic Ventures IV-STOCK-6
Al_2O_3	43.30	42.55 – 44.06	0.41	Jadeite
Cr_2O_3	0.07	0 – 0.25	0.08	Cr_2O_3
CaO	1.17	1.10 – 1.20	0.03	Wollastonite
MnO**	0.40	0.21 – 0.64	0.12	$MnTiO_3$
FeO**	0.14	0.02 – 0.30	0.10	Fe_2O_3
PbO	0.36	0.31 – 0.39	0.03	PbTe
Li_2O*	1.65			Inorganic Ventures IV-STOCK-6
Na_2O	1.04	0.93 – 1.20	0.08	Jadeite
F	0.89	0.77 – 0.93	0.05	CaF_2
H_2O***	3.04			
O=F	– 0.37			
Total	**99.57**			

*From ICP-AES

**All Mn and Fe considered as MnO and FeO, respectively, for classification purposes. The green color of the associated fluor-elbaite is likely due to Fe^{2+} (Bosi *et al.*, 2013)

*** calculated from 0.338 wt.% H determined by CHN-analysis.

Table 2. Powder X-ray diffraction data (d in Å) for fluor-rossmanite.

hkl	d_{obs}	I_{obs}	d_{calc}	I_{calc}
1 1 0	7.883	15	7.898	11
0 1 -1	6.304	10	6.292	13
0 2 1	4.929	8	4.921	15
3 0 0	4.555	6	4.560	9
2 1 1	**4.181**	**22**	**4.177**	**17**
2 2 0	**3.941**	**100**	**3.949**	**100**
0 1 2	3.431	9	3.430	14
1 3 1	3.347	7	3.345	5
4 1 0	2.980	8	2.985	6
1 2 2	**2.930**	**39**	**2.923**	**47**
5 0 -1	**2.552**	**25**	**2.552**	**29**
0 0 3	2.363	11	2.362	7
2 3 2	2.349	5	2.349	8
5 1 1	2.319	12	2.321	14
0 5 -2	2.163	8	2.165	5
4 3 1	2.146	12	2.143	7
4 2 2	2.088	12	2.088	6
5 1 -2	**2.017**	**16**	**2.019**	**22**
3 4 2	**1.894**	**15**	**1.899**	**20**
0 6 3	**1.640**	**18**	**1.640**	**11**
2 7 1	1.625	12	1.627	10
5 5 0	**1.580**	**15**	**1.580**	**19**

Note: The eight strongest reflections are shown in bold. Only reflections with a relative intensity ≥ 5 are reported.

Table 3. Data from single-crystal X-ray diffraction analysis and structure refinement.

Crystal data	
Crystal size (mm)	$0.25 \times 0.15 \times 0.05$
Crystal system	trigonal
Space group	$R3m$
Unit cell dimensions (Å)	$a = 15.7951(3)$ $c = 7.08646(17)$
Volume (Å^3)	$V = 1531.11(7)$
Z	3
Density (g/cm^3) (calculated)	3.074
Data collection and refinement	
Instrument	Supernova Rigaku Oxford Diffraction
Radiation, wavelength (Å), temperature (K)	Mo$K\alpha$, 0.71073, 298(2)
2θ range (°)	5.16 to 63.2
Total reflections	9133
Unique ref (all)	1178
Unique ref [$I > 2\sigma(I)$]	1167
R_{int}	0.0302
Range of h, k, l	$-22 \leqslant h \leqslant 23,\ -22 \leqslant k \leqslant 22,\ -10 \leqslant l \leqslant 9$
R_1, wR_2 [$I > 2\sigma(I)$]	$R_1 = 0.0211,\ wR_2 = 0.0563$
R_1 [all data]	$R_1 = 0.0212$
Goodness-of-fit	1.124
Data/restraints/parameters	1178/0/90
Maximum and minimum residual peak (e Å^{-3})	0.49 -0.57

Weighting scheme: w =1/[s^2(Fo^2)+(0.0364×P)^2+0.6233×P] where P = (Fo^2 + 2Fc^2)/3

Table 4. Atom coordinates and equivalent anisotropic displacement parameters U_{eq} (in Å^2) (the complete list of anisotropic displacement parameters is provided with the CIF).

Sites	x/a	y/b	z/c	U_{eq}
X	0	0	0.2270(5)	0.0192(10)
Y	0.12207(10)	0.06104(5)	0.6367(2)	0.0079(4)
Z	0.29681(5)	0.26026(5)	0.60848(15)	0.00582(15)
T	0.19152(4)	0.18962(5)	0	0.00630(14)
B	0.10901(13)	0.2180(3)	0.4528(5)	0.0056(6)
F1(W)	0	0	0.7763(7)	0.0335(11)
O2	0.06032(9)	0.12064(19)	0.4889(4)	0.0135(6)
O3(V)	0.2626(2)	0.13129(11)	0.5067(4)	0.0122(5)
O4	0.09377(10)	0.1875(2)	0.0733(4)	0.0096(5)
O5	0.1870(2)	0.09349(10)	0.0954(4)	0.0102(5)
O6	0.19472(12)	0.18427(12)	0.7744(3)	0.0075(3)
O7	0.28644(12)	0.28610(12)	0.0768(3)	0.0070(3)
O8	0.20943(13)	0.27002(13)	0.4381(3)	0.0071(3)

Table 5. Selected interatomic distances (Å) for fluor-rossmanite.

X – O2	2.483(4)x3		**Y – F1**	1.941(3)
X – O5	2.722(3)x3		**Y – O6**	1.956(2)x2
X – O4	2.787(3)x3		**Y – O2**	1.963(2)x2
<X – O>	2.664		**Y – O3**	2.132(3)
			<Y – O>	1.985
Z – O6	1.8677(19)		**T – O6**	1.603(2)
Z – O7	1.8805(18)		**T – O7**	1.6067(17)
Z – O8	1.8835(18)		**T – O4**	1.6137(11)
Z – O8′	1.8974(18)		**T – O5**	1.6306(13)
Z – O7′	1.9362(17)		**<T – O>**	1.614
Z – O3	1.9650(14)			
<Z – O>	1.905			
			B – O2	1.356(4)
			B – O8	1.378(3)x2
			<B – O>	1.371

21

Table 6. Bond valence values for fluor-rossmanite.

	X	*Y*	*Z*	*T*	*B*	Σ
F1(W)		0.349×3				1.047
O2	0.104×3	0.370×2			1.033	1.877
O3(V)		0.244	0.429×2			1.102
O4	0.049×3			1.038×2		2.125
O5	0.058×3			0.992×2		2.042
O6		0.376×2	0.553	1.069		1.998
O7			0.535 0.463	1.058		2.056
O8			0.530 0.513		0.976	2.019
BVS	0.633	2.085	3.023	4.157	2.985	

Note: F1 was calculated considering 44% and 56% O. *Y* and *T* sites were calculated using the cation population from the experimental chemical formula. BVS = Bond-Valence Sum. In order to perform the bond valence calculation, we used the mean R_0 and B_0 values from the following references: Brown and Altermatt, 1985; Urusov, 2006; Yu and Xue, 2006; Cabana *et al.*, 2004; Brese and O'Keeffe, 1991; Czervinska *et al.*, 2016; Gagne and Hawthorne, 2015; Adams, 2001; Kanowitz and Palenik, 1998; Liu and Thorp, 1993; Allmann, 1975; Krivovichev and Brown, 2001; Wood and Palenik, 1999).

Table 7. Proportions of individual end-members in fluor-rossmanite.

General formula arrangement				Fraction, mol.%	End-member component
$^X\square^0$	$^Y(Li^{1+}R^{3+}_2)$	$^ZAl^{3+}_6$ $^TSi^{4+}_6$	$O_{18}(BO_3)_3{}^V(OH)_3{}^WX^{1-}$	46	fluor-rossmanite
$^XNa^{1+}$	$^Y(Li^{1+}R^{3+}_2)$	$^ZAl^{3+}_6$ $^TSi^{4+}_6$	$O_{18}(BO_3)_3{}^V(OH)_3{}^WO^{2-}$	32	darrellhenryite
$^XR^{2+}$	$^Y(Li^{1+}_2R^{3+})$	$^ZAl^{3+}_6$ $^TSi^{4+}_6$	$O_{18}(BO_3)_3{}^V(OH)_3{}^WX^{1-}$	13.5	liddicoatite
$^XR^{2+}$	$^YR^{3+}_3$	$^ZAl^{3+}_6$ $^T(Al^{3+}_4Si^{4+}_2)$	$O_{18}(BO_3)_3{}^V(OH)_3{}^WX^{1-}$	4.5	$CaAl_3Al_6(Al_4Si_2)O_{18}(BO_3)_3(OH)_3(OH)$
$^XR^{2+}$	$^YR^{2+}_3$	$^ZAl^{3+}_6$ $^TSi^{4+}_6$	$O_{18}(BO_3)_3{}^V(OH)_3{}^WO$	2.33	$CaMn^{2+}_3Al_6Si_6O_{18}(BO_3)_3(OH)_3O$
$^XR^{2+}$	$^YR^{3+}_3$	$^ZAl^{3+}_6$ $^T(Si^{4+}_3Al^{3+}_3)$	$O_{18}(BO_3)_3{}^V(OH)_3{}^WO$	0.67	$R^{2+}Al_3Al_6(Al_3Si_3)O_{18}(BO_3)_3(OH)_3O$
$^XR^{2+}$	$^YTi^{4+}_3$	$^ZAl^{3+}_6$ $^TAl^{3+}_6$	$O_{18}(BO_3)_3{}^V(OH)_3{}^WO$	0.16	$R^{2+}Ti^{4+}_3Al_6Al_6O_{18}(BO_3)_3(OH)_3O$

$^XR^{2+}$=Ca, Pb; $^YR^{2+}$=Mn^{2+}, Fe^{2+}; $^YR^{3+}$=Al^{3+}, Cr^{3+}; $^WX^{1-}$=F$^-$, OH^{-1}

Note. The symbols R and X indicate that more elements of the same charge were involved in endmember calculations. Unequivocally defined elements are depicted by their chemical symbols.

22

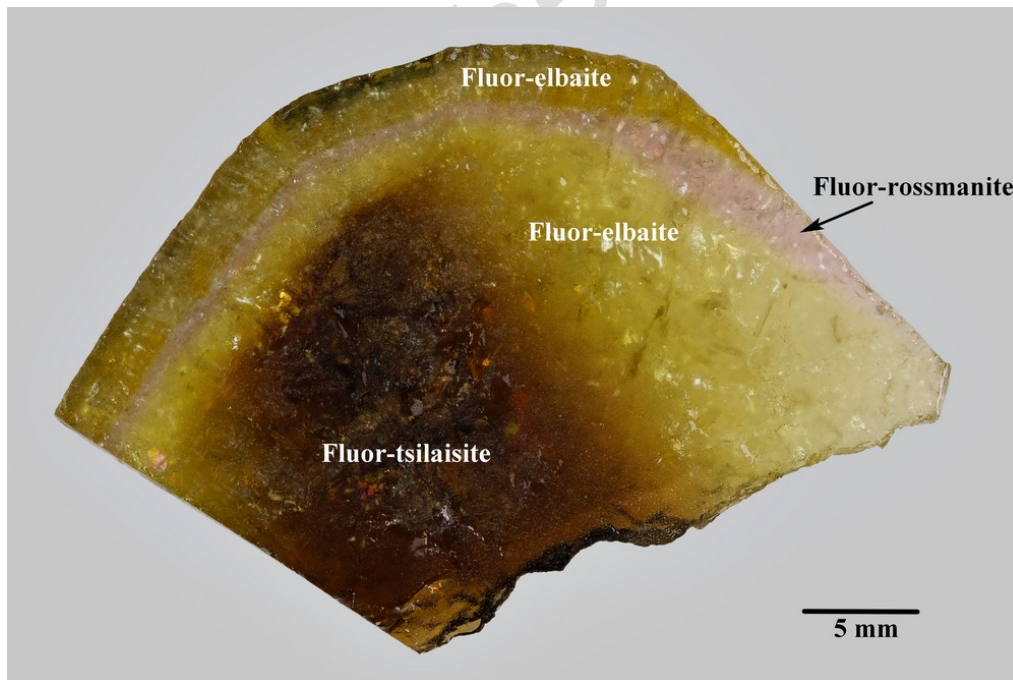**Figure 1:** Krutaya pegmatite, Malkhan pegmatite field. Field of view ~16 m x 8 m. Photo by E. E. Novoselova, summer 2021.

Figure 2. Cross section of polychrome tourmaline crystal with fluor-rossmanite zone. Photo by Maria D. Milshina. Specimen no. 6049/1.
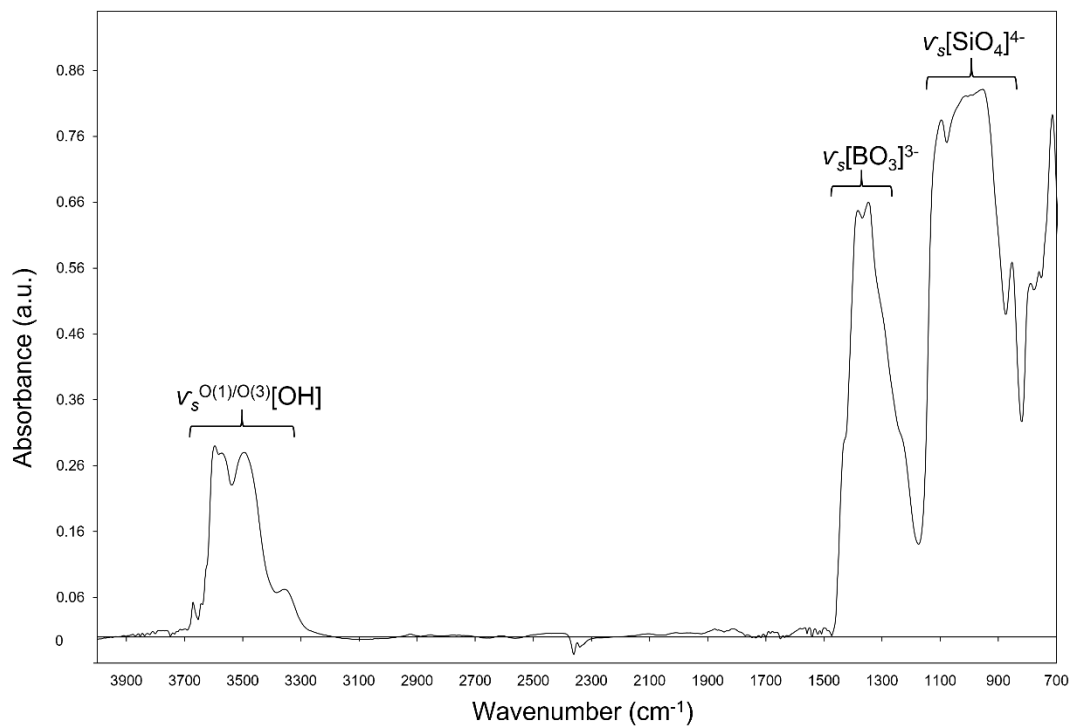.

23

Figure 3. The FTIR spectrum of fluor-rossmanite in the range 4000–700 cm^{-1}. Bands are observed that are associated with $^{O(1)/O(3)}$[OH]-stretching modes, [BO$_3$]$^{3-}$ and [SiO$_4$]$^{4-}$ stretching and bending modes.
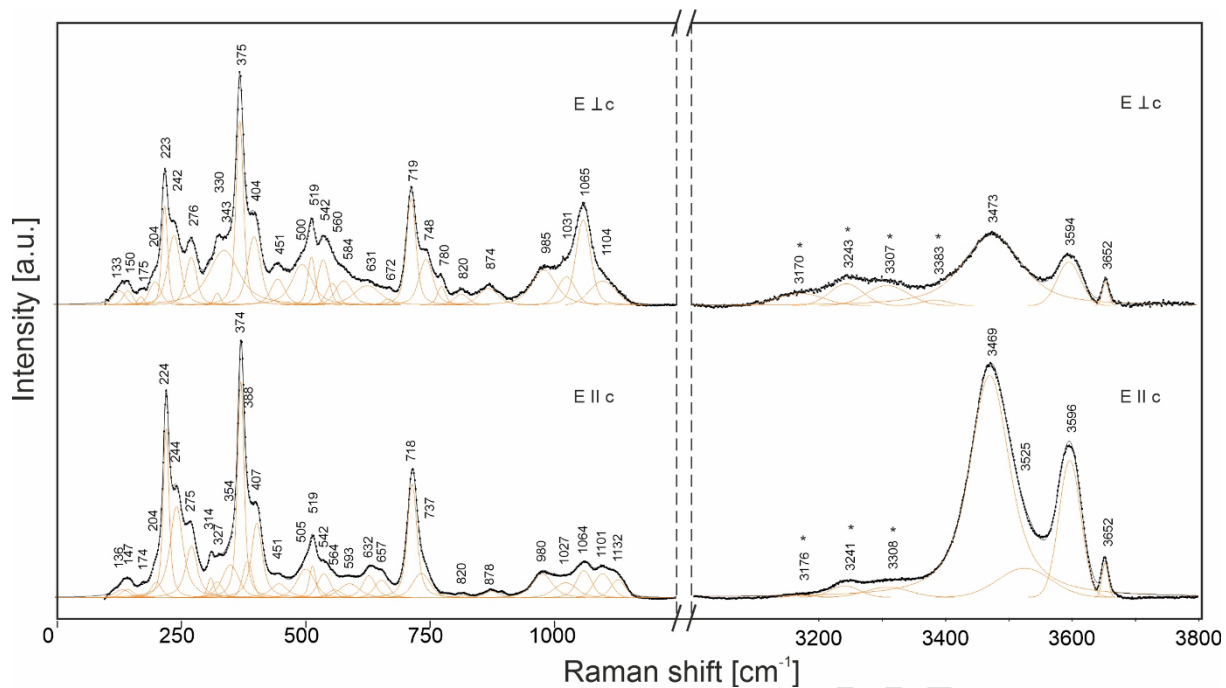
24

Figure 4. The Raman spectrum of fluor-rossmanite in the range of 80-1250 cm^{-1} and 3000-3800 cm^{-1} excited by a 532 nm laser. The upper spectrum corresponds to the orientation of the tourmaline *c* axis perpendicular to the laser polarization, the lower spectrum corresponds to orientation of the *c* axis parallel to the laser polarization. The measured spectrum is shown with a dashed line. All observed peaks were fit with Voigt functions and the resultant fit-line (sum) is shown with a solid black line. The luminescence peaks are marked with an asterisk.